Magnetic excitations of the gapped quantum spin dimer antiferromagnet $Sr_3Cr_2O_8$

D. L. Quintero-Castro,[1,2,*] B. Lake,[1,2] E. M. Wheeler,[1] A. T. M. N. Islam,[1] T. Guidi,[3] K. C. Rule,[1] Z. Izaola,[1] M. Russina,[1] K. Kiefer,[1] and Y. Skourski[4]

[1]*Helmholtz Zentrum Berlin für Materialien und Energie, D-14109 Berlin, Germany*

[2]*Institut für Festkörperphysik, Technische Universität Berlin, D-10623 Berlin, Germany*

[3]*ISIS Facility, Rutherford Appleton Laboratory, Chilton, Didcot, Oxon OX11 0QX, United Kingdom*

[4]*Hochfeld Magnetlab, Forschungszentrum Dresden-Rossendorf EV, D-01314 Dresden, Germany*

(Received 21 September 2009; revised manuscript received 17 November 2009; published 21 January 2010)

$Sr_3Cr_2O_8$ consist of a lattice of spin-1/2 Cr^{5+} ions, which form hexagonal bilayers and which are paired into dimers by the dominant antiferromagnetic intrabilayer coupling. The dimers are coupled three dimensionally by frustrated interdimer interactions. A structural distortion from hexagonal to monoclinic leads to orbital order and lifts the frustration giving rise to spatially anisotropic exchange interactions. We have grown large single crystals of $Sr_3Cr_2O_8$ and have performed DC susceptibility, high-field magnetization and inelastic neutron scattering measurements. The neutron scattering experiments reveal three gapped and dispersive singlet to triplet modes arising from the three twinned domains that form below the transition thus confirming the picture of orbital ordering. The exchange interactions are extracted by comparing the data to a random phase approximation model and the dimer coupling is found to be $J_0=5.551(9)$ meV, while the ratio of interdimer to intradimer exchange constants is $J'/J_0=0.64(2)$. The results are compared to those for other gapped magnets.

DOI: 10.1103/PhysRevB.81.014415 PACS number(s): 75.10.Jm, 75.25.−j

I. INTRODUCTION

Over the last decade, many exotic quantum phenomena have been observed in spin dimer systems. For example $TlCuCl_3$, which consists of spin-1/2 dimers coupled in a three-dimensional lattice, has a spin-singlet ground state and a gapped dispersive one-magnon excited state. Application of a magnetic field causes Bose-Einstein condensation of magnons at a critical field H_c, while for higher-fields magnetization increases smoothly to saturation.[1,2] $BaCuSi_2O_6$ consists of Cu^{2+} ions arranged on a bilayer of square lattices with unfrustrated antiferromagnetic couplings. The intrabilayer coupling is dominant so that the system can be regarded as a square lattice of dimers. The ground state is again a singlet, the excitations are dispersive gapped magnons[3,4] and as for $TlCuCl_3$, magnetization increases smoothly above a critical field. The spin-1/2 Shastry-Sutherland antiferromagnet $SrCu_2(BO_3)_2$ consists of spin-1/2 dimers arranged at right angles to each other so that the interdimer couplings are competing. The ground state is again a singlet and the excitations form a gapped mode whose dispersion bandwidth is suppressed by frustration.[5] Magnetization is characterized by a critical field and for higher fields a series of magnetization plateaux are found where the condensed magnons form superlattices with spontaneous breaking of translation symmetry known as Wigner crystallization.[6]

Recently, a new set of dimerized antiferromagnets with formula $A_3M_2O_8$ (A=Ba,Sr and M=Mn,Cr) have been investigated. In these compounds the magnetic ion (Mn or Cr) is in the 5^+ oxidation state leading to spin-1 in the case of Mn^{5+} and spin-1/2 in the case of Cr^{5+}. These compounds crystallize in a hexagonal structure with space group $R\bar{3}m$ at room temperature. The magnetic ions lie on hexagonal bilayers where the dominant intrabilayer interaction is antiferromagnetic and gives rise to the dimerization. These dimers are coupled three dimensionally, both within the bilayers and between bilayers to give a highly frustrated arrangement. $Ba_3Mn_2O_8$ maintains the hexagonal structure down to the lowest temperatures. Stone *et al.*[7,8] found that the magnetic excitations are gapped, dispersive magnon modes typical of a dimerized magnet. Magnetic exchange constants have been extracted by fitting the single mode approximation to the data,[7] and by spin dimer analysis based on a extended Hückel tight binding calculation.[9] The magnetization shows two magnetic plateaux.[10] The first is due to a triplet condensation into the ground state and the second is a quintet condensation. Critical properties of $Ba_3Mn_2O_8$ have also been extensively studied by Suh and Samulon[11,12] who find that the critical points can be defined as a Bose Einstein condensation of magnons tuned by an external magnetic field.

In the case of $Ba_3Cr_2O_8$ and $Sr_3Cr_2O_8$, the unusual 5^+ valence state of Chromium results in a single electron in the $3d$ shell. The Cr^{5+} ion is surrounded by an oxygen tetrahedron and this crystal field splits the $3d$ levels so that electron occupies the doubly-degenerate lower lying e orbitals. The Cr^{5+} ion in this environment is thus Jahn-Teller active and a Jahn-Teller distortion would lift both the orbital degeneracy and magnetic frustration. Although a lowering of the bulk crystal symmetry has not been found in $Ba_3Cr_2O_8$ neutron powder diffraction reveals anomolous behavior of the displacement parameters of the apical oxygen below 100 K suggesting a local Jahn-Teller distortion.[13] Furthermore three gapped and dispersive excitation branches were observed in inelastic neutron scattering, corresponding to the three twinned domains that form below the transition.[13] The magnetic excitations were fitted by a random phase approximation (RPA) model and the interdimer couplings were shown to be spatially anisotropic as would be expected in the monoclinic phase.[13] The magnetization was also consistent with gapped excitations showing zero magnetization up to $H_c=12.5$ T and then a smooth increase up to saturation at $H_s=23.6$ T.[14,15] A combination of neutron diffraction, heat ca-

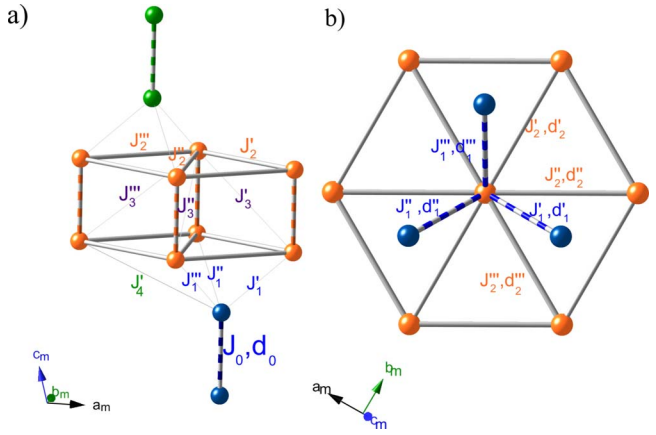

FIG. 1. (Color online) The low temperature (monoclinic) crystal structure of $Sr_3Cr_2O_8$ giving the magnetic Cr^{5+} ions only. (a) Shows the bilayer structure, (b) Shows the "hexagonal" plane. The exchange interactions and Cr^{5+}-Cr^{5+} distances are labeled on the diagram.

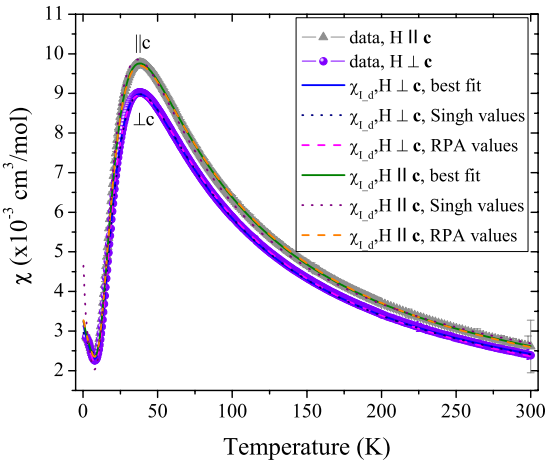

FIG. 2. (Color online) Static susceptibility data measured using the SQUID magnetometer for field applied both parallel and perpendicular to c_h displayed along with the fitted interacting dimer model given by Eq. (1).

pacity, magnetocaloric effect and magnetic torque measurements were performed at high-magnetic fields to map out the phase diagram as a function of field and temperature around the critical fields.[14,15] The extracted critical exponents were found to be consistent with theoretical predictions for three-dimensional Bose-Einstein condensation at H_c although not at H_s.

Here, we investigate the magnetic properties of $Sr_3Cr_2O_8$, which has very recently also been found to show Bose-Einstein condensation behavior.[16] The room temperature crystal structure of $Sr_3Cr_2O_8$ was solved in 1989 by Cuno and Müller and found to be hexagonal with space group $R\bar{3}m$.[17] A decade later the thermodynamic properties were investigated by Jacob,[18] but their samples were shown by x-ray absorption near edge structure to have a mixed valence state. Much more recently Singh *et al.*[19] measured DC magnetic susceptibility and heat capacity on polycrystalline samples. The susceptibility revealed a spin-singlet ground state and could be fitted by a model of weakly coupled dimers with an intradimer exchange constant of 5.34 meV at base temperature, while the specific heat confirmed the absence of long range magnetic order in this compound. Chapon *et al.* performed powder neutron diffraction and found that $Sr_3Cr_2O_8$ undergoes a structural phase transition below 275 K to a monoclinic structure with space group $C2/c$.[20] The transition is thought to be a cooperative Jahn-Teller distortion that lifts the degeneracy of the e orbitals, stabilizing the $3z^2-r^2$ orbital at lower energy than the x^2-y^2 and giving rise to antiferro-orbital ordering. This ordering alters the magnetic exchange paths and lifts the magnetic frustration. At room temperature in the hexagonal phase the lattice parameters are $a_h=b_h=5.57$ Å, $c_h=20.17$ Å while at 1.6 K in the monoclinic phase the lattice parameters are: $a_m=9.66$ Å, $b_m=5.5437$ Å, $c_m=13.7882$ Å, and $\beta=103.66°$. The subscript "h" denotes hexagonal notation and "m" monoclinic.

Figure 1 shows the network of Cr^{5+} ions forming the structure of $Sr_3Cr_2O_8$. The hexagonal layers lie in the (a_h,b_h) plane and are paired into bilayers in the c_h direction. These bilayers are in turn stacked along c_h in a repeated *ABCABC* pattern. The shortest Cr^{5+}-Cr^{5+} distance is the first neighbor intrabilayer distance [labeled d_0 in Fig. 1(a)] and the corresponding coupling constant is J_0. In the high-temperature hexagonal phase the Cr^{5+} ions, within the hexagonal layers, are separated by distance d_2 and are coupled by the exchange constant J_2. However, below the structural distortion the hexagonal distances become unequal (labeled d_2', d_2'', d_2''' in Fig. 1) corresponding to three different exchange interactions J_2', J_2'', and J_2'''. The same is true for the third neighbor intrabilayer exchange constant and the interbilayer interactions. These spatially anisotropic exchange interactions would result in crystal twinning since there are three possible ways, in which the hexagonal symmetry can be broken to form the monoclinc structure (see Table I).

In this paper, we investigate the magnetic properties of $Sr_3Cr_2O_8$. We study the system using DC susceptibility, high-field magnetization and inelastic neutron scattering on both powder and single crystal samples. We show that $Sr_3Cr_2O_8$ is indeed a dimerized magnet with $J_0=5.551(9)$ meV and substantial three-dimensional interdimer couplings. The neutron scattering data reveal three excitation modes corresponding to the three twinned domains, thus, confirming the Jahn-Teller distortion and the spatially anisotropic exchange interactions that arise at this transition. The data are compared to a RPA model and the exchange constants are determined. The results are compared to those for $Ba_3Mn_2O_8$ and $Ba_3Cr_2O_8$ and are discussed in relation to other gapped magnets.

II. EXPERIMENTAL DETAILS

Single crystalline samples of $Sr_3Cr_2O_8$ were growth in the Crystal Laboratory at the Helmholtz Zentrum Berlin für Materialien und Energie (HZB) in Berlin, Germany. The initial powders were synthesized by a solid state reaction. Stoichiometric amounts of $SrCO_3$ (99.994% purity, Alfa Aesar) and Cr_2O_3 (99.97% purity, Alfa Aesar) were mixed thoroughly,

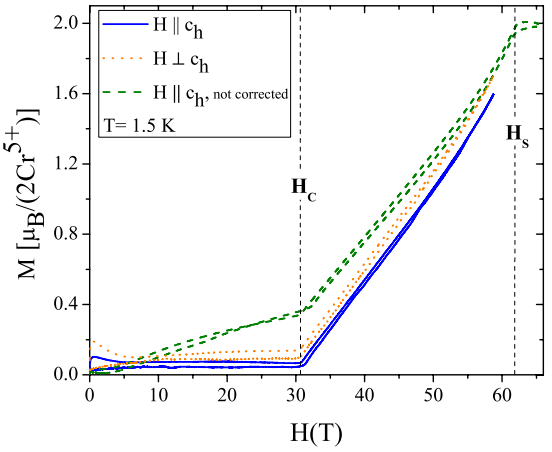

FIG. 3. (Color online) Magnetization per $2Cr^{5+}$ ions as a function of applied magnetic field. This measurement was performed using a pulsed magnet at base temperature $T=1.5$ K and field applied both parallel and perpendicular to c_h. The data represented by the green line is not background corrected.

pressed into a pellet and heated first for 24 h at 850 °C and then for 24 h at 1250 °C (with intermediate grindings). The powders were quenched to avoid the formation of other phases such as $SrCrO_4$ and $Sr_{10}Cr_6O_{24}(OH)_2$ and were then pressed into a feed rod using a cold isostatic press (EPSI Inc.). The single crystal growth was performed by the floating zone technique, using a high-temperature optical floating zone furnace (Crystal Systems Inc. Model FZ-T-10000-H-VI-VPO). An atmosphere of synthetic air was used to maintain the correct level of oxygen needed for the high-oxidation state of the Cr^{5+} and to reduce the moisture level to prevent the growth of other phases. The resulting samples were typically cylindrical with diameter ≈6 mm and length 35–50 mm. Further details of the growth of $Sr_3Cr_2O_8$ are given in Ref. 21.

The static magnetic susceptibility and low-field magnetization of $Sr_3Cr_2O_8$ were measured using a superconducting quantum interference device (Magnetic Property Measurement System, Quantum Design) at the Laboratory for Magnetic Measurements, HZB. The samples had a volume of 3 mm^3 and the data were collected with a magnetic field applied both parallel and perpendicular to c_h. The susceptibility measurements were performed using a field of 3 T over a temperature range of 2–300 K. The high-field magnetization of $Sr_3Cr_2O_8$ was measured using a pulsed inductive magnetometer at the Hoch-Feld Institute in Dresden. The measurements took place over a field range of 0–65 T and a variety of temperatures from 1.5 to 50 K, again both field directions ($H \perp c_h$ and $H \| c_h$) were measured.

The magnetic excitation spectrum was investigated using inelastic neutron scattering. For an overview of the excitation spectrum, powder measurements were performed on the cold multi-disc-chopper neutron time-of-flight spectrometer *V3 -NEAT* at the BER II reactor, HZB. The polycrystalline sample (mass=9.5 g) was inserted into a cylindrical aluminum container and mounted inside a standard orange cryostat. Data were collected for incident wavelengths (energies) of 2 Å(20.45 meV), 2.5 Å(13.09 meV), and 3.2 Å(7.99 meV), resulting in a resolution at the elastic line (at 5.3 meV energy transfer) of 1.437 meV (1.053 meV), 0.742 meV (0.448 meV), and 0.442 meV (0.187 meV), respectively. All the data were collected at 2 K and each scan was counted for approximately 20 h. A vanadium standard was used for the detector normalization and empty can measurements were used for the background subtraction.

For a detailed study of the magnetic dispersion, two types of single crystal inelastic neutron scattering measurements were performed. First, using MERLIN,[22] a direct geometry time-of-flight spectrometer at the ISIS facility, Rutherford Appleton Laboratory, U.K. and second the cold-neutron triple-axis-spectrometer V2-FLEX at HZB. The MERLIN experiment allowed the magnetic excitations to be measured over a large range of energy and wave vector transfer and provided an overview of the spectrum. Three single crystals of total mass 10 g were co-aligned with the c_h axis vertical and cooled in a closed cycle cryostat to a base temperature of 6 K. A Fermi chopper was phased to select neutrons with an incident energy of 10 meV and was spun at a frequency of

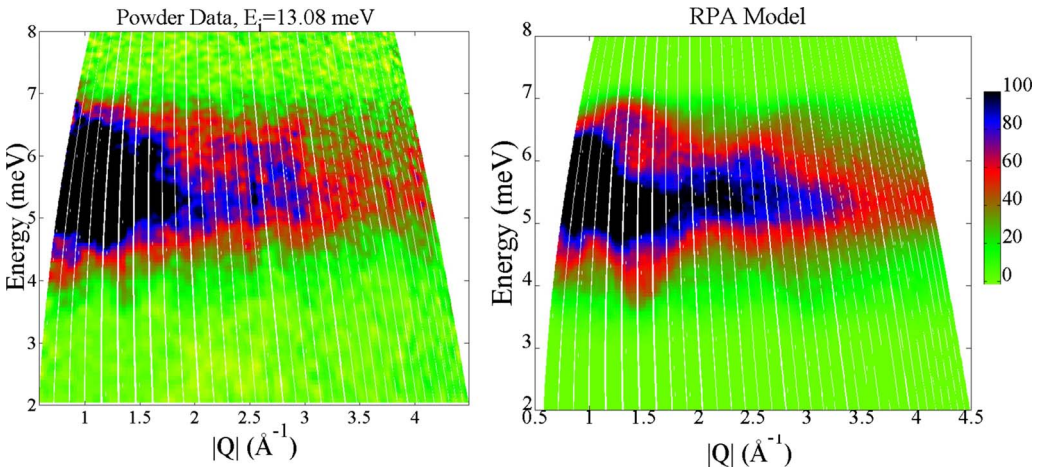

FIG. 4. (Color online) The left panel shows the inelastic neutron scattering data measured on a powder sample. The data was collected on NEAT at 2 K and the incident energy was 13.08 meV. The intensity is in arbitrary units. The right panel shows the RPA simulation over the same energy and wave vector ranges.

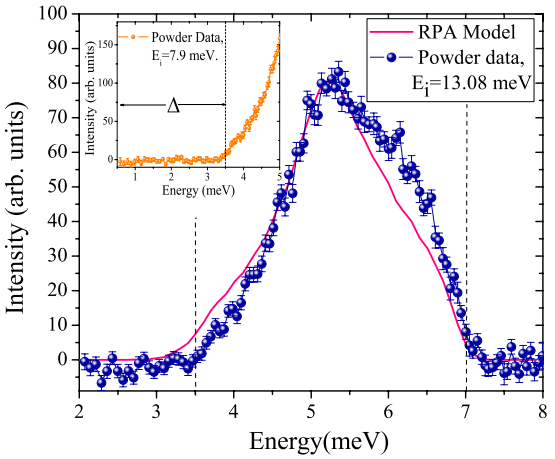

FIG. 5. (Color online) The data (blue circles) and RPA simulation (solid magenta line) from Fig. 4, integrated over the wave-vector range $1.5<|Q|<3.5$ Å^{-1} and plotted as a function of energy. The dashed vertical lines indicate the bandwidth of the excitations. The inset shows the lower energy region and reveal the clean energy gap (Δ), this data was taken with an incident energy of 7.9 meV and the cut is over the wave vector range of $0.6<|Q|<1.5$ Å^{-1}.

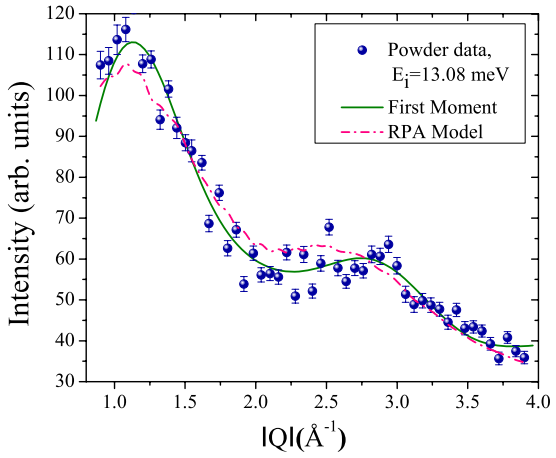

FIG. 6. (Color online) The data (blue circles) and RPA simulation (dot-dashed magenta line) from Fig. 4, multiplied by energy transfer and integrated over energy. The solid green line gives the fit to the first moment sum rule, Eq. (6).

100 Hz to achieve a resolution at the elastic line of 0.37 meV. An omega scan was performed where the sample was rotated about the vertical axis in steps of 1° covering an angular range of 70° with a counting time of 2 h per step. A vanadium standard was used to normalize the individual measurements for detector efficiency and then the full data set was combined using the program Horace[23] to give the excitation spectrum over a large volume of reciprocal space and energy transfer.

The measurements performed on V2-FLEX were used to obtain high-resolution data for accurate mapping of the dispersion relations. Two separate experiments were performed. For the first, a single crystal (mass=3.7 g) was oriented with the $(h_h,0_h,\ell_h)$ plane as the instrumental scattering plane. For the second experiment two co-aligned single crystals (total mass=7.7 g) were used to investigate the (h_h,h_h,ℓ_h) plane. An orange cryostat was used to cool the sample and most of the measurements were performed at 2 K. A vertically focusing Pyrolitic graphite (PG) monochromator and horizontally focusing PG analyzer selected the incident and final energies, respectively. While a nitrogen-cooled beryllium filter was used between the sample and analyzer to remove $\lambda/2$ and higher order reflections from the monochromator. The instrument was operated in the W-configuration (+−+) and the collimator settings were guide-60′-open-open. The measurements were performed with fixed final wave vectors of $k_f=1.2$ Å^{-1} (2.98 meV) and $k_f=1.55$ Å^{-1} (4.98 meV). The resolution of the instrument, determined from the full-width-half-maximum (FWHM) of the incoherent scattering was 0.09 meV for $k_f=1.2$ Å^{-1} and 0.12 meV for a $k_f=1.55$ Å^{-1}. Constant-wave vector scans were used to map out the magnon dispersions from 0–8 meV in steps of 0.05 meV. The average counting time was 4 min per point.

III. RESULTS AND DISCUSSION

A. Static Susceptibility

The DC susceptibility of $Sr_3Cr_2O_8$ is displayed in Fig. 2. The figure shows the susceptibility with the field applied both perpendicular and parallel to c_h, the two curves are slightly different suggesting a weakly anisotropic g tensor as found for $Ba_3Cr_2O_8$.[15] The results reveal a broad maximum at 38 K and a sharp drop toward zero at lower temperatures as found in the previous powder measurement.[19] Such a susceptibility curve is characteristic of a dimerized magnet with a singlet ground state and gapped magnetic excitations. The susceptibility rises again at very low temperatures presumably due to paramagnetic impurities. Note, however, that this paramagnetic tail is smaller than in the previous measurement[19] suggesting a higher quality sample. Altogether we expect three contributions to the susceptibility,

$$\chi_{\text{obs}} = \chi_0 + \chi_{\text{imp}} + \chi_{\text{interacting-dimer}}. \tag{1}$$

The temperature independent term, χ_0, is due to Van Vleck paramagnetism and diamagnetic core susceptibility and is expected to give a small contribution $\sim 10^{-4}$ cm^3/mol. The second term, χ_{imp}, is due to paramagnetic impurities, which are responsible for the Curie tail at low temperatures and has the form:

$$\chi_{\text{imp}} = \frac{C_{\text{imp}}}{T-\theta_{\text{imp}}}, \tag{2}$$

where C_{imp} is the Curie constant of the impurities and θ_{imp} is their Curie-Weiss temperature. The third term, $\chi_{\text{interacting-dimer}}$, is due to the coupled dimer arrangement proposed for $Sr_3Cr_2O_8$ and is modeled by

$$\chi_{\text{interacting-dimer}} = \frac{3C/T}{[3+e^{(J_0/k_BT)}+J'/T]}. \tag{3}$$

This expression is described in Refs. 19 and 24. It is derived from the Bleaney-Bowers equation for spin-1/2 dimers coupled by Heisenberg intradimer exchange constant J_0, and

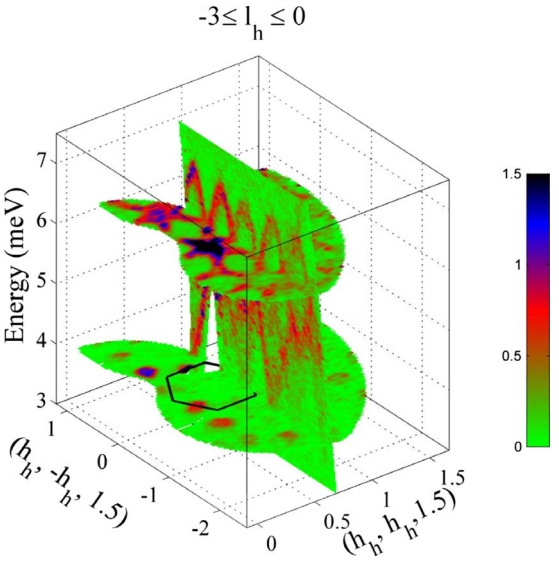

FIG. 7. (Color online) Sections of the MERLIN data set displaying the dispersion as a function of energy and wavevector in the hexagonal (a_h^*, b_h^*)-plane and integrated over c_h^*, from −3 to 0 r.l.u. The solid black hexagon indicates the hexagonal Brillouin zone. The intensity is in arbitrary units.

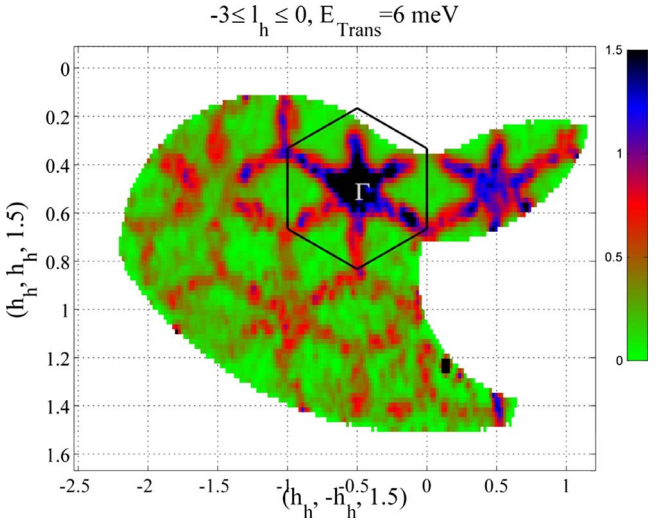

FIG. 8. (Color online) Slice showing the scattering for energy transfer 5.9 meV as a function of wave vector in the hexagonal (a_h^*, b_h^*)-plane, integrated over c_h^*, from −3 to 0 r.l.u. The solid black hexagon indicates the hexagonal Brillouin zone. The intensity is in arbitrary units.

J' is the effective field on each spin due to its couplings with the neighboring spins. In the case of unfrustrated interdimer couplings J' is simply the sum of the modulus of these couplings, which for $Sr_3Cr_2O_8$ would be $J' = (|J_1'| + |J_1''| + |J_1'''|) + 2(|J_2'| + |J_2''| + |J_2'''|) + 2(|J_3'| + |J_3''| + |J_3'''|) + (|J_4'| + |J_4''| + |J_4'''|)$. However, if the interactions are competing due to frustration they act against each other reducing the size of J'. The constant C is the Curie constant of this system.

The measured susceptibility data was fitted to Eq. (1) and good agreement was found over the full temperature range, see Fig. 2. The fitted parameters for the data with the field perpendicular to the c_h axis are $\chi_0 = 2.32(5) \times 10^{-4}$ cm^3/mol, $C_{\text{imp}} = 0.0465(5)$ cm^3 K/mol, $\theta_{\text{imp}} = -15.7(2)$ K, $C = 0.875(2)$ cm^3 K/mol, $J_0 = 5.517(2)$ meV, and $J' = 1.3(8)$ meV. The value of C corresponds to an effective moment of $1.8(1)\mu_B/\text{Cr}^{5+}$, which is close to the value of $1.72\mu_B$ expected for spin-1/2 Cr^{5+} ions assuming a g factor of 1.98 taken from a previous electron paramagnetic resonance (EPR) measurement of Cr doped $ZrSiO_4$.[25] The values obtained from fitting the susceptibility data with the field parallel to the c_h axis are: $\chi_0 = 1.76(5) \times 10^{-4}$ cm^3/mol, $C_{\text{imp}} = 0.0481(6)$ cm^3 K/mol, $\theta_{\text{imp}} = -15.3(3)$ K, $C = 0.987(2)$ cm^3 K/mol, $J_0 = 5.512(3)$ meV, $J' = 2.0(3)$ meV, giving $\mu_{\text{eff}} = 1.9(1)\mu_B/\text{Cr}^{5+}$.

Our values for the intradimer and interdimer exchange interactions can be compared to the values of $J_0 = 5.17(1)$ meV and $J' = 0.5(2)$ meV found previously by Singh *et al.*[19] While our fitted intradimer exchange constant is in good agreement, our value of the interdimer coupling is much greater. If the values of J_0 and J' are however fixed to those of Singh *et al.*[19] we obtain a fit that is almost as good as shown in Fig. 2. Furthermore, the values of $J_0 = 5.551(9)$ meV and $J' = 3.6(1)$ meV, obtained by fitting our inelastic neutron scattering data to a RPA model as described later in the text, where the size of J' was found to be much larger, gave equally good agreement with the data. Altogether our susceptibility agrees well with a model of interacting spin-1/2 dimers and gives an intradimer exchange constant of $J_0 \approx 5.5$ meV. However, it is unable to give accurate information about the interdimer exchange coupling and for that information we turn first to magnetization and then inelastic neutron scattering.

B. High-field magnetization

The high-field magnetization of $Sr_3Cr_2O_8$ reveals three distinct regions, see Fig. 3. Below the critical field of $H_c = 30.9(4)$ T there is zero magnetization (the gradual increase in magnetization observed in the 65 T measurement (green line) is because this data has not been background corrected). Between H_c and $H_s = 61.9(3)$ T the magnetization increases rapidly and smoothly, while above H_s a magnetization plateau is observed at $M_s = 1.97(3)\mu_B/2\text{Cr}^{5+}$. This is identified as the saturation plateau since it is very close to the theoretical value of $2g_s\mu_B S = 1.98\mu_B/2\text{Cr}^{5+}$ (assuming $g = 1.984$).

The observed magnetization can be explained within the proposed interacting dimer model of $Sr_3Cr_2O_8$. In this model the ground state is a singlet resulting in no magnetization at low magnetic fields. The excitations would form a gapped magnon mode, which disperses between an upper and lower energy. The magnons possess a spin of $S = 1$ and their triplet degeneracy is lifted by an applied magnetic field. The critical field corresponds to a Zeeman energy such that the gap is closed by the $S^z = 1$ magnons which start to populate the ground state; from this we can deduce that $E_{\text{gap}} = g_s\mu_B H_c = 3.54(5)$ meV. The saturation field corresponds to the ground state being fully occupied by excited dimers. The size of this field can be used to calculate an approximate value for the upper edge of the dispersion assuming that magnon-

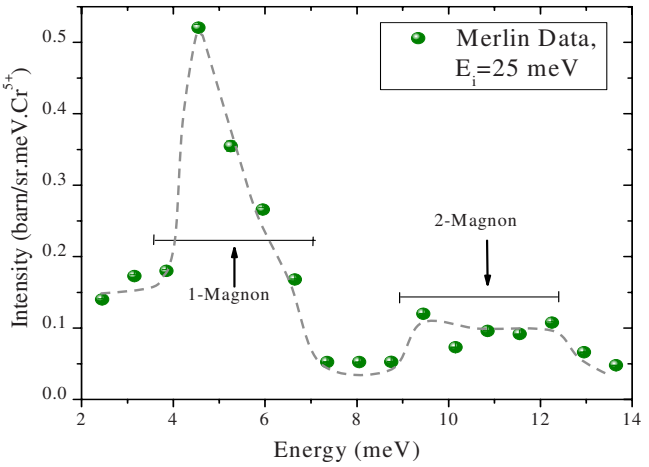

FIG. 9. (Color online) one and two-magnon scattering measured at $T=6$ K with incident neutrons of energy 25 meV pointing in the $(h_h,h_h,0_h)$ direction. The data is integrated over the wave vector ranges $-0.2<h_h<0.2$, $-1<k_h<1$, $-1<\ell_h<1$. Lines are guides to the eye.

magnon interactions are weak or cancel, if this is the case $E_{\text{upper}}\approx g_s\mu_B H_s=7.09(4)$ meV.

The magnetization data are therefore consistent with the model of interacting spin-1/2 dimers and suggests that the excitations are centered around ≈5.3 meV and disperse over a bandwidth of ≈3.55 meV. Since in unfrustrated dimerized magnets the bandwidth is equal to J' (the sum of the modulus of the interdimer exchange constants) the significant bandwidth revealed by the magnetization suggests substantial interdimer couplings with $J'\approx 3.55$ meV. Finally, it should be noted that the absence of any intermediate magnetization plateau is in contrast to the findings for some other gapped magnets that are highly frustrated e.g., $SrCu_2(BO_3)_2$ which has steps in its magnetization.[6] This result is however in agreement with related compound $Ba_3Cr_2O_8$.[26]

C. Powder inelastic neutron scattering

In order to learn more about the magnetic excitations of $Sr_3Cr_2O_8$, we performed inelastic neutron scattering measurements on a powder sample. Figure 4 shows data collected on NEAT at 2 K plotted as a function of wave vector transfer $|Q|$ and energy transfer E. The spectrum reveals a band of gapped excitations centered at ~5.5 meV. The measured neutron scattering intensity reduces with increasing $|Q|$ confirming the magnetic nature of the excitations. Figure 5 gives the spectrum integrated over the wave vector range $1.5<|Q|<3.5$ Å^{-1} and plotted as a function of energy, and clearly shows that within resolution, $E_{\text{gap}}=3.4(3)$ meV and $E_{\text{upper}}=7.10(5)$ meV. These results are in good agreement with the values obtained from our magnetization measurements and confirm the picture of interacting dimers giving rise to gapped and dispersive magnon excitations. Additional measurements using a smaller incident energy of 7.99 meV were performed to probe the lower energy region more carefully and confirm the complete absence of magnetic scattering below 3.5 meV as shown in the inset of Fig. 5.

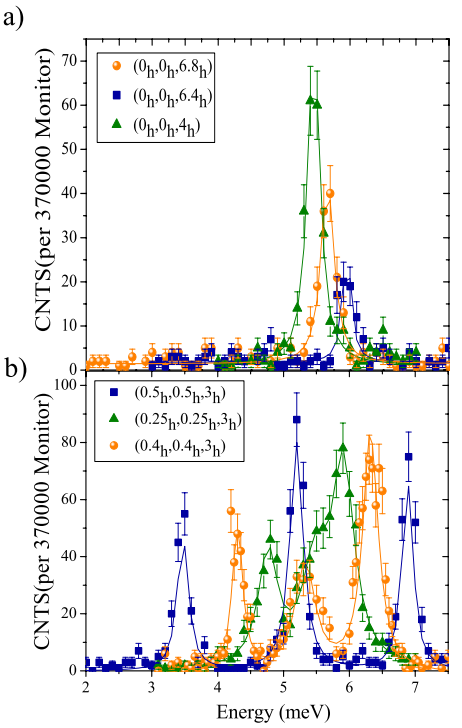

FIG. 10. (Color online) Constant-wave vector scans in the (a) $(0_h,0_h,\ell_h)$ and (b) $(h_h,h_h,3_h)$ directions measured at 2 K. The solid lines are fits to Lorentzian functions.

The $|Q|$ averaging due to the powder sample prevents exact determination of the dispersion relations; however some information can be gained by looking at the lower edge of the excitation band. A minimum in the excitation spectrum occurs at $|Q|=0.87$ Å^{-1}, which corresponds to the reciprocal lattice point $(1/2_h,0_h,1_h)$, and further minima are observed e.g., at $|Q|=1.48$ Å^{-1} suggesting that the minima of the dispersion occur at $(h_h/2,0_h,\ell_h)$ where h_h and ℓ_h are integer, as well as symmetry equivalent positions.

Information about the relative importance of the various magnetic couplings in $Sr_3Cr_2O_8$ can be extracted from the data by using the first moment sum rule.[27] For an isotropic spin system where the magnetic ions are coupled by Heisenberg exchange interactions, the first moment $\langle E\rangle$ of the scattering function, $S(Q,\omega)$, is given by

$$\langle E\rangle=\hbar^2\int_{\omega=-\infty}^{\infty}\omega S(\mathbf{Q},\omega)d\omega$$

$$\propto-\sum_i J_i\langle\mathbf{S}_0\cdot\mathbf{S}_{d_i}\rangle[1-\cos(\mathbf{Q}\cdot\mathbf{d}_i)]. \quad (4)$$

In this equation J_i is the exchange constant coupling the i-th nearest-neighbor spins, d_i is their separation and $|\langle\mathbf{S}_0\cdot\mathbf{S}_{d_i}\rangle|$ is the two spin correlation function for this pair. From this expression it is clear that each coupling constant J_i produces a modulation in the first moment with a periodicity depending on the separation d_i of the spins. Thus by fitting this expression to the first moment of the data it should be possible to identify the dominant exchange paths.

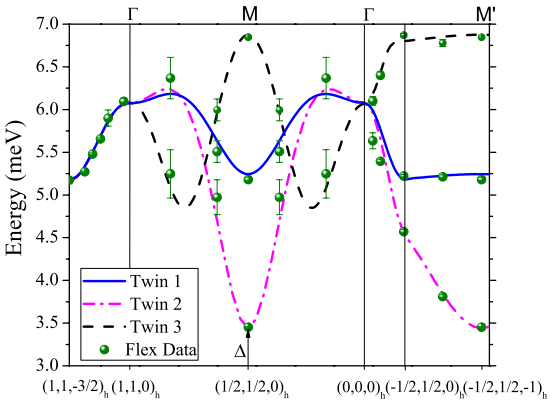

FIG. 11. (Color online) Dispersion relation. The blue, magenta and black lines correspond to the fitted dispersion relations of the three monoclinic twins. The green points are the fitted centers of the peaks measured on FLEX. The wave vectors on the x-axis are labeled using the hexagonal notation.

For comparison to the powder measurement of $Sr_3Cr_2O_8$ it is necessary to take the powder average and include the magnetic form factor of Cr^{5+}, $f_{Cr^{5+}}(|Q|)$, such that

$$\langle E\rangle \propto \sum_i J_i \langle \mathbf{S}_0 \cdot \mathbf{S}_i\rangle |f_{Cr^{5+}}(|Q|)|^2 \left(1 - \frac{\sin(|Q||d_i|)}{|Q||d_i|}\right). \quad (5)$$

The possible interactions for the monoclinic phase of $Sr_3Cr_2O_8$ are illustrated in Fig. 1, however, since the set of distances d_i', d_i'' and d_i''' $(i \neq 0)$ are almost equal it is not possible to distinguish between them in the fitting and we therefore replace these distances by the average distance d_i (d_0=3.8448 Å, d_1=4.3172 Å, d_2 =5.5718 Å, d_3=6.7696 Å). The expression then becomes

$$\langle E\rangle \propto -\sum_{i=0}^{3} A_i |f_{Cr^{5+}}(|Q|)|^2 \left(1 - \frac{\sin(|Q||d_i|)}{|Q||d_i|}\right). \quad (6)$$

Where the terms A_0 and A_i are

$$A_0 = J_0 \langle \mathbf{S}_0 \cdot \mathbf{S}_{d_0}\rangle \quad (7)$$

$$A_i = J_i' \langle \mathbf{S}_0 \cdot \mathbf{S}_{d_i'}\rangle + J_i'' \langle \mathbf{S}_0 \cdot \mathbf{S}_{d_i''}\rangle + J_i''' \langle \mathbf{S}_0 \cdot \mathbf{S}_{d_i'''}\rangle. \quad (8)$$

An expression for the form factor of Cr^{5+} could not be found in the literature, we therefore estimated it by extrapolation from the known form factors for Cr^{4+} and V^{4+} to be

$$|f_{Cr^{5+}}(|Q|)|^2 = |Ae^{-as^2} + Be^{-bs^2} + Ce^{-cs^2} + D|^2, \quad (9)$$

where $s=|Q|/4\pi$ and the constants are $A=-0.2602$, $a=0.03958$, $B=0.33655$, $b=15.24915$, $C=0.90596$, $c=3.2568$, and $D=0.0159$. The data, multiplied by energy transfer and integrated over the energy to give the first moment is shown in Fig. 6 as a function of wave vector. The theoretical expression in Eq. (6) was then fitted by varying the quantities A_i and the best fit, shown by the green line, corresponds to the fitted values A_0=402(3), A_1=−24(5), A_2 =−24(4), and A_3=−45(4).

The results reveal that, as expected, the dominant exchange constant of $Sr_3Cr_2O_8$, which is responsible for coupling the spins into dimers is the intrabilayer interaction, J_0. Indeed, the quantity A_0 is more that an order of magnitude greater than the other A_i values, clearly identifying it as the main interaction. Unfortunately, it is not possible to obtain the absolute values of the exchange constants using this method as the fitted quantities also depend on the spin correlation functions. Nevertheless, it is clear that there are significant interdimer interactions and that $Sr_3Cr_2O_8$ can be viewed as a network of dimers coupled both along the c_h axis and within the distorted "hexagonal" plane. These results can be compared to the inelastic neutron scattering measurements of Chapon *et al.*,[20] which were also performed on a powder sample. A gapped band of excitations was observed centered at an energy of 5.46 meV in agreement with our data. The FWHM of this band was found to be 2.1 meV although values of the gap and upper boundary were not found due to the poorer energy resolution of their measurement.

In order to gain more information about the exchange paths in $Sr_3Cr_2O_8$ it is necessary to measure the magnon dispersions along specific directions in reciprocal space, since only in this way can the set of interactions J_i', J_i'', and

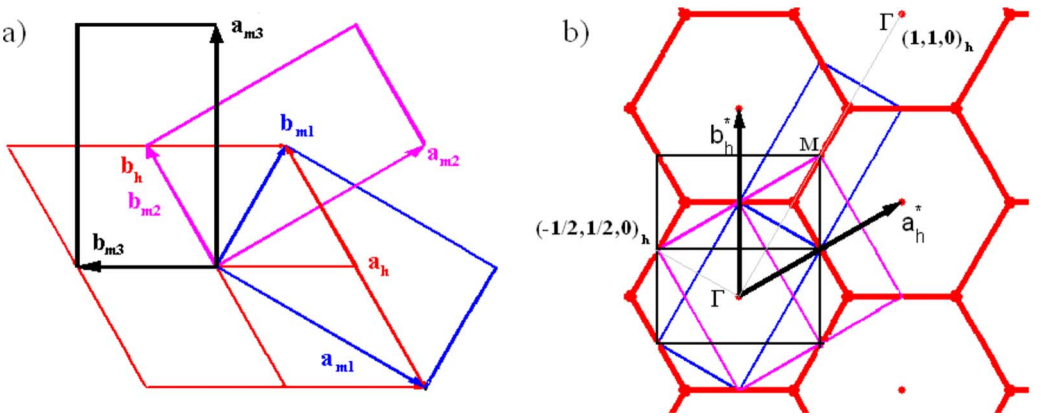

FIG. 12. (Color online) (a) Relationship between the hexagonal and monoclinic real spaces. Red thick: hexagonal lattice. Blue: lattice of monoclinic twin 1. Magenta: monoclinic twin 2. Black: monoclinic twin 3. (b) Relationship between the hexagonal and monoclinic reciprocal spaces, projected onto the hexagonal plane, using the same color coding.

TABLE I. The relationship between the hexagonal lattice parameters and those of the three monoclinic twins is given as well as the relationship between the hexagonal and monoclinic reciprocal spaces.

Real Space			
Twin1 (a_{m1},b_{m1},c_{m1})	$a_{m1}=a_h-b_h$	$b_{m1}=a_h+b_h$	$c_{m1}=a_h/3-b_h/3+2c_h3$
Twin2 (a_{m2},b_{m2},c_{m2})	$a_{m2}=2a_h+b_h$	$b_{m2}=b_h$	$c_{m2}=2a_h/3+b_h/3+2c_h3$
Twin3 (a_{m3},b_{m3},c_{m3})	$a_{m3}=a_h+2b_h$	$b_{m3}=-a_h$	$c_{m3}=a_h/3+2b_h/3+2c_h3$
Reciprocal Space			
Twin1 $(a^*_{m1},b^*_{m1},c^*_{m1})$	$a^*_{m1}=a^*_h/2-b^*_h/2-c^*_h/2$	$b^*_{m1}=a^*_h/2+b^*_h/2$	$c^*_{m1}=3c^*_h/2$
Twin2 $(a^*_{m2},b^*_{m2},c^*_{m2})$	$a^*_{m2}=a^*_h/2-c^*_h/2$	$b^*_{m2}=-a^*_h/2+b^*_h$	$c^*_{m2}=3c^*_h/2$
Twin3 $(a^*_{m3},b^*_{m3},c^*_{m3})$	$a^*_{m3}=b^*_h/2-c^*_h/2$	$b^*_{m3}=-a^*_h+b^*_h/2$	$c^*_{m3}=3c^*_h/2$

J_i''' be distinguished from each other and their values accurately determined. This can be achieved by inelastic neutron scattering measurements from a single crystal sample which is the subject of the next section.

D. Single crystal inelastic neutron scattering

1. MERLIN data

Single crystal inelastic neutron scattering experiments were performed at 6 K on the MERLIN spectrometer allowing us to measure the magnetic excitations over a large region of reciprocal space. Figures 7 and 8 show slices through this data set where the intensity has been summed over the range $-3<\ell_h<0$. Figure 7 shows the full extent of the dispersion and Fig. 8 shows the measured intensity at a constant energy transfer of 6 meV. A complicated excitation spectrum is revealed consisting of three excitation branches. The presence of three modes rather than one confirms the Jahn-Teller distortion proposed by Chapon *et al.*[20] from diffraction measurements. This structural phase transition gives rise to three monoclinic twins each of which produces a separate mode. In agreement with the powder data, the dispersion curves have a gap of 3.4 meV and a maximum energy of 6.9 meV. The minima and the maxima occur at the midpoints of the faces of the hexagonal Brillouin zone, equivalent to $(1/2_h,1/2_h,0_h)$.

In addition to the observed one-magnon scattering, two-magnon scattering is also expected where the neutron creates two magnons simultaneously. Such scattering would be centered at twice the average one-magnon energy ($\approx$10.4 meV) and with a bandwidth that is the same as the one-magnon bandwidth (8.7–12.1 meV). The two magnon cross-section is expected to be considerably weaker than the one-magnon cross-section, but nevertheless observable. Figure 9 shows the measured scattering intensity as a function of energy transfer integrated over the wave vector range $-0.2<h_h<0.2$, $-1<k_h<1$, $-1<\ell_h<1$. In this region of reciprocal space, the intensity of the two-magnon scattering is strongest while that of the one-magnon is weak. The two magnon peak is clearly observable at $\approx$10.5 meV. Both one and two-magnon signal show some structure because of the limited integration range of the data.

2. V2-Flex data

In order to make an accurate determination of the exchange constants, high-resolution single crystal inelastic neutron scattering experiments at 2 K were performed using V2-FLEX. The excitation spectrum was mapped out by scanning the energy transfer at constant wave vector within the $(h_h,0_h,\ell_h)$ and (h_h,h_h,ℓ_h) planes. Key scans are shown in Fig. 10. As found for the MERLIN data, three peaks were observed at general wave vectors corresponding to the three twinned domains see Fig. 10(b). These excitations disperse in all directions showing that the interdimer couplings are three dimensional. The branches merge together in the center of the hexagonal Brillouin zone (Γ point), and are degenerate when h_h and k_h are integer so that a single mode is observed as a function of ℓ_h see Fig. 10(a). The bandwidth of the dispersion in this direction gives the interbilayer coupling.

The peaks were fitted to Lorentzians to obtain their positions, (solid lines in Fig. 10) and, thus, map out the dispersion relations of the three twinned domains as a function of energy and wave vector. Figure 11 illustrates the dispersions in various reciprocal lattice directions. The green circles give the excitation energies extracted from each scan and the lines are fits to the RPA model, which will be explained in the next section. The three lines (magenta, black, and blue) represent the three twins, which are rotated by 60° with respect to each other about the c^*_h-axis. The dispersion of Twin 1 (blue line) is the same as that of Twin 2 (magenta line) 60° away in reciprocal space and the same as that of Twin 3 (black line) 120° away.

The relationship between the hexagonal structure and three monoclinic twins is given in Table I where the transformations for both the real and reciprocal lattices are listed. Figure 12 illustrates these relationships projected onto the "hexagonal" plane, where the original hexagonal lattice is draw in red, and the monoclinic twins are shown in blue, magenta, and black. From Fig. 12(b) it is clear that the corners of the monoclinic Brillouin zones sit at the midpoints of the faces of the hexagonal Brillouin zone (M points). For example, the M point at $(1/2_h,1/2_h,0_h)$ is at the corner of the Brillouin zone of monoclinic Twins 2 and 3, but is at the center of the Brillouin zone of Twin 1. At this wave vector the peak from Twin 2 is at the dispersion minimum while that from Twin 3 is at the dispersion maximum and that from

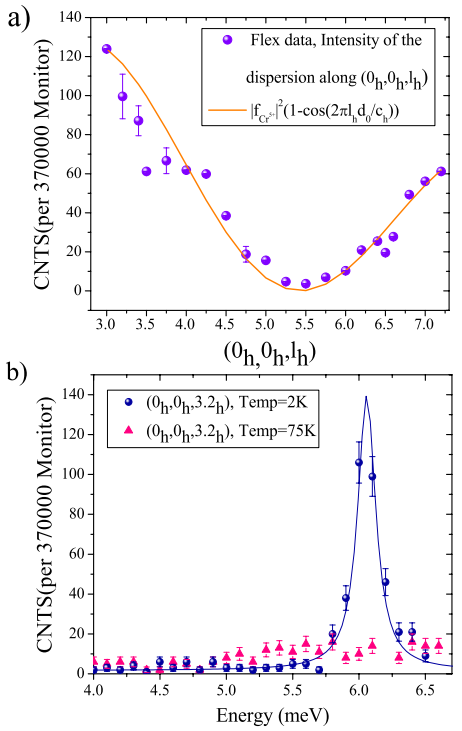

FIG. 13. (Color online) (a) Fitted intensity of the magnon in the $(0_h,0_h,\ell_h)$ direction. (b) Comparison of the peak at $\boldsymbol{Q}=(0_h,0_h,3.2_h)$ at 2 and 75 K.

Twin 1 is at the center of the bandwidth, see Fig. 11. An equivalent way to generate the twins is by permuting each set of exchange constants $\{J_i',J_i'',J_i'''\}$, in this way the dispersion of Twin 1 can be transformed into that of the other two twins.

In a strongly dimerized system such as $Sr_3Cr_2O_8$ the intensity of the excitations is dominated by the dimer structure factor which is of the form:

$$|f_{Cr^{5+}}(|Q|)|^2[1-\cos(2\pi\ell_h d_0/c_h)]. \tag{10}$$

Since the dimer separation d_0 is parallel to the c_h axis we expect an intensity modulation as a function of wave vector transfer along ℓ_h. The colored symbols in Fig. 13(a) show the intensity of the excitations in the $(0_h,0_h,\ell_h)$ direction extracted by fitting the peaks observed in the energy scans [Fig. 10(a)] to Lorentzians. The intensity is found to modulate with a distinctive minimum at $\ell_h=5.5$ r.l.u., and comparison to the theoretical expression (orange line) suggests that the dimer separation is $c_h/5.5=3.67$ Å in good agreement with the nearest neighbor Cr^{5+}-Cr^{5+} distance $d_0=3.7140(4)$ Å. This modulation therefore provides yet further evidence that $Sr_3Cr_2O_8$ is a system of coupled dimers.[28] Finally, we performed a higher temperature measurement at 75 K. Figure 13(b) shows the comparison between the data at 2 K and 75 K which is well above the temperature of the maximum in the magnetic susceptibility (see Fig. 2). At 75 K most of the intensity has vanished clarifying the magnetic origin of this excitation.

IV. ANALYSIS

In order to develop a better understanding of the exchange interactions in $Sr_3Cr_2O_8$ we compared the extracted dispersion relations to a RPA calculation based on the dimer unit. In this model the dispersion relation is[13]

$$\hbar\omega \cong \sqrt{J_0^2 + J_0\gamma(\mathbf{Q})}, \tag{11}$$

$$\gamma(\mathbf{Q}) = \sum_i J(\mathbf{R_i})e^{-i\mathbf{Q}\cdot\mathbf{R_i}}, \tag{12}$$

where $\gamma(Q)$ is the Fourier sum of the interdimer interactions. For monoclinic twin 1, $\gamma(Q)$ is given by

$$\begin{aligned}\gamma(h_h,k_h,\ell_h)_{\text{Twin1}} &= 2J_1'\cos\left[\frac{2}{3}\pi(2h_h+k_h+\ell_h)\right]\\ &+ 2J_1''\cos\left[\frac{2}{3}\pi(-h_h+k_h+\ell_h)\right]\\ &+ 2J_1'''\cos\left[\frac{2}{3}\pi(-h_h-2k_h+\ell_h)\right]\\ &+ 2(J_2'-J_3')\cos(2\pi h_h)\\ &+ 2(J_2''-J_3'')\cos(2\pi k_h)\\ &+ 2(J_2'''-J_3''')\cos[2\pi(h_h+k_h)]\\ &+ 2J_4'\cos\left[\frac{2}{3}\pi(2h_h+4k_h+\ell_h)\right]\\ &+ 2J_4''\cos\left[\frac{2}{3}\pi(2h_h-2k_h+\ell_h)\right]\\ &+ 2J_4'''\cos\left[\frac{2}{3}\pi(-4h_h-2k_h+\ell_h)\right],\end{aligned} \tag{13}$$

where we have included the set of fourth-order interactions J_4', J_4'', and J_4''', which were found to be significant in the analysis of $Ba_3Mn_2O_8$. Note that in this model, it is not possible to distinguish between the sets J_2', J_2'', J_2''' and J_3', J_3'', J_3''' and only the difference between these exchange parameters matters i.e., $J_2'-J_3'$ etc. Also note that the minus sign expresses the fact that J_2' and J_3' compete if they have the same sign (e.g., both antiferromagnetic) but reinforce each other if they have different signs. $\gamma(Q)$ for the other twins can be generated from that of twin 1 by permuting the exchange constants as follows

$$\begin{aligned}\{J'_{1,2-3,4},J''_{1,2-3,4},J'''_{1,2-3,4}\}_{\text{Twin1}} &\rightarrow \{J''_{1,2-3,4},J'''_{1,2-3,4},J'_{1,2-3,4}\}_{\text{Twin2}}\\ &\rightarrow \{J'''_{1,2-3,4},J'_{1,2-3,4},J''_{1,2-3,4}\}_{\text{Twin3}}.\end{aligned}$$

In this way the magnetic excitations for all three twins can be calculated. The RPA model was compared to the dispersion relations extracted from the V2-FLEX data (see Fig. 11). In these experiments the excitations were measured in two planes the $(h_h,0_h,\ell_h)$ and (h_h,h_h,ℓ_h) and for these specific planes Eq. (13) reduces to:

TABLE II. The exchange constants in units of meV extracted from the RPA model, compared to the values for $Ba_3Cr_2O_8$ and $Ba_3Mn_2O_8$. Antiferromagnetic interactions are positive while ferromagnetic interactions are negative.

Exchange Constants	$Sr_3Cr_2O_8$	$Ba_3Cr_2O_8$ [a]	$Ba_3Mn_2O_8$ [b]
J_0	5.551(9)	2.38	1.642
J_1'	−0.04(1)	−0.15	−0.118
J_1''	0.24(1)	0.08	−0.118
J_1'''	0.25(1)	0.10	−0.118
$J_2'-J_3'$	0.751(9)	0.10	0.256−0.142
$J_2''-J_3''$	−0.543(9)	−0.52	0.256−0.142
$J_2'''-J_3'''$	−0.120(9)	0.07	0.256−0.142
J_4'	0.10(2)	0.10	−0.037
J_4''	−0.05(1)	0.04	−0.037
J_4'''	0.04(1)	0.09	−0.037
$J'=\lvert J_1'\rvert+\lvert J_1''\rvert+\lvert J_1'''\rvert+\lvert J_4'\rvert+\lvert J_4''\rvert+\lvert J_4'''\rvert$	$J'=3.6(1)$	$J'=1.94$	$J'=1.147$
$+2(\lvert J_2'-J_3'\rvert)+2(\lvert J_2''-J_3''\rvert)+2(\lvert J_2'''-J_3'''\rvert)$	$J'/J_0=0.64(2)$	$J'/J_0=0.8151$	$J'/J_0=0.6983$

[a]Reference 13.
[b]Reference 7.

$$\gamma(h_h,0_h,\ell_h)_{Twin1} = 2J_1'\cos\left[\frac{2}{3}\pi(2h_h+\ell_h)\right] + (2J_1''+2J_1''')\cos\left[\frac{2}{3}\pi(-h_h+\ell_h)\right] + [2(J_2'-J_3')+2(J_2'''-J_3''')]\cos(2\pi h_h) + 2(J_2''-J_3'') + (2J_4'+2J_4'')\cos\left[\frac{2}{3}\pi(2h_h+\ell_h)\right] + 2J_4'''\cos\left[\frac{2}{3}\pi(-4h_h+\ell_h)\right] \quad (14)$$

and

$$\gamma(h_h,h_h,\ell_h)_{Twin1} = 2J_1'\cos\left[\frac{2}{3}\pi(3h_h+\ell_h)\right] + 2J_1''\cos\left[\frac{2}{3}\pi(\ell_h)\right] + 2J_1'''\cos\left[\frac{2}{3}\pi(-3h_h+\ell_h)\right] + 2[(J_2'-J_3')+2(J_2''-J_3'')]\cos(2\pi h_h) + 2(J_2'''-J_3''')\cos(4\pi h_h) + 2J_4'\cos\left[\frac{2}{3}\pi(6h_h+\ell_h)\right] + 2J_4''\cos\left(\frac{2}{3}\pi\ell_h\right) + 2J_4'''\cos\left[\frac{2}{3}\pi(-6h_h+\ell_h)\right]. \quad (15)$$

These equations can be simplified further if scans along key directions are considered, e.g., for directions where h_h and k_h are integers and ℓ_h varies, the set of interactions $J_2'-J_3'$, $J_2''-J_3''$, $J_2'''-J_3'''$ do not modulate the structure but only give an overall constant, thus allowing us to obtain the interactions J_0, J_1', J_1'', J_1''' and J_4', J_4'', J_4'''. The directions with h_h and k_h half integer were then used to get the values for $J_2'-J_3'$, $J_2''-J_3''$, $J_2'''-J_3'''$. The fitted exchange constants are listed in Table II and the resulting dispersion relations for the three monoclinic twins are illustrated in Fig. 11 and clearly show that this model provides a good approximation to the data.

The neutron scattering cross-section from these modes can also be calculated in the RPA model and is given by

$$\frac{d^2\sigma(\mathbf{Q},E)}{d\Omega dE} \approx \frac{|f_{Cr^{5+}}(|Q|)|^2\left[1-\cos\left(\frac{2\pi\ell_h d_0}{c_h}\right)\right]e^{[-(E-\hbar\omega)^2/\Delta E^2]}}{\hbar\omega(1-e^{E/k_BT})}. \quad (16)$$

Where E is the energy transfer, ΔE is the energy resolution of the instrument, which is assumed to be Gaussian and T is the temperature. The cosine term comes from the structure factor of a single dimer [see Eq. (10)]. Using the fitted values of the exchange constants (from Table II), a simulation was performed of the MERLIN experiment. Figure 14 shows good agreement between the data and the simulation for various slices. The RPA model along with the fitted exchange constants was also used to reproduce the data from the inelastic powder measurement performed on V3-NEAT as shown in Fig. 4 (right panel). Cuts as a function of energy and wave vector were performed on this simulation and compare well to the data see Figs. 5 and 6. Finally, the fitted interactions were used to calculate the effective field $J'=3.6(1)$ meV (see Table II), which was used along with the fitted value of J_0 to simulate our susceptibility data using Eq. (3). This simulation is shown in Fig. 2 and is consistent with the data.

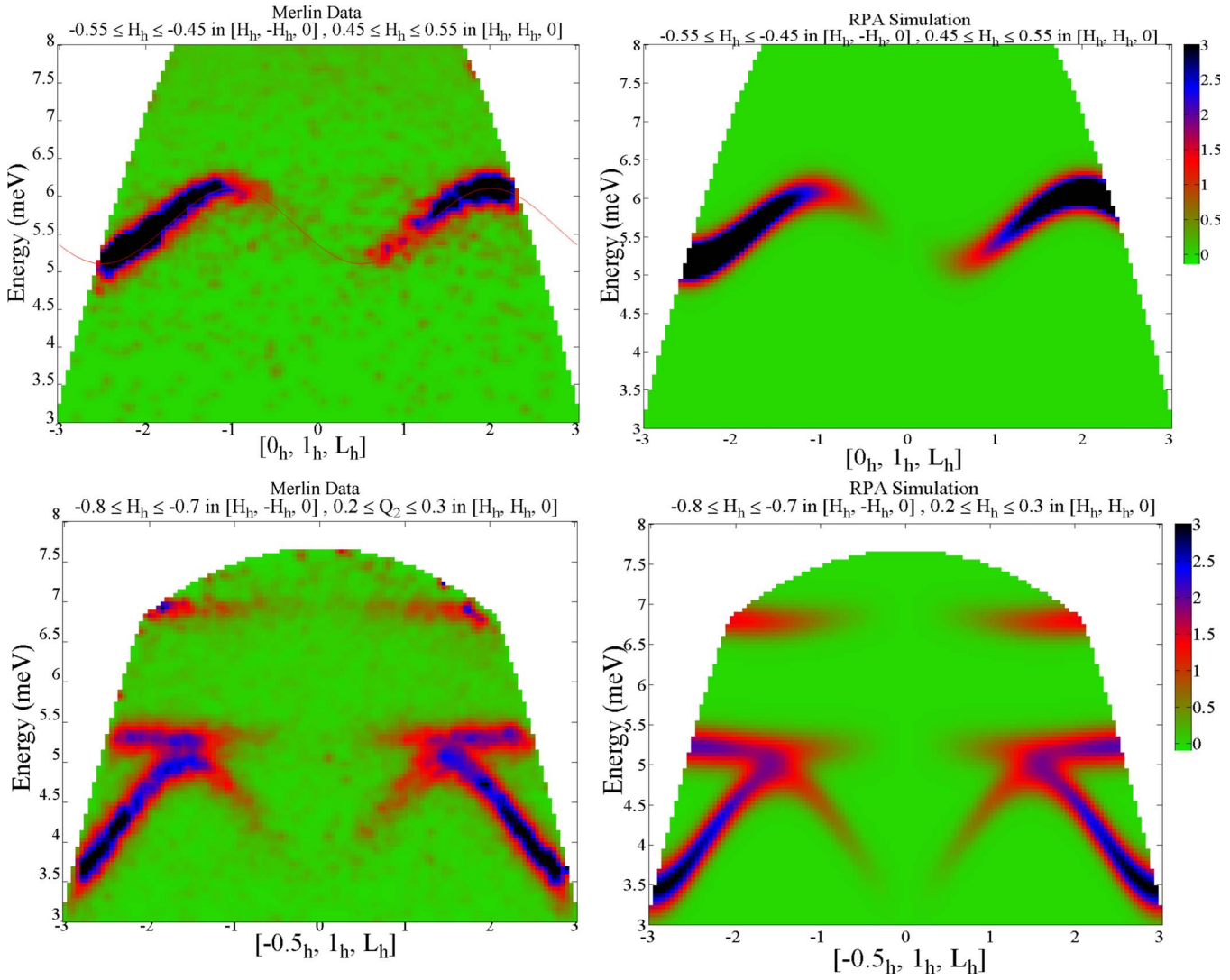

FIG. 14. (Color online) Shows slices of the MERLIN Data (left panels) and the RPA simulation (right panels) for the directions $(0_h, 1_h, \ell_h)$ and $(-0.5_h, 1_h, \ell_h)$, with $E_i = 10$ meV and 6 K. The intensity is in arbitrary units.

V. DISCUSSION

Our DC susceptibility, high-field magnetization and inelastic neutron scattering results provide a consistent picture of $Sr_3Cr_2O_8$ as a dimerized spin-1/2 antiferromagnet. The intradimer exchange constant is identified as the intrabilayer interaction J_0, which has a value of 5.551(9) meV as found from both susceptibility and inelastic neutron scattering. This dimerization gives rise to a singlet ground state and gapped one-magnon excitations. There are in addition significant interdimer interactions that allow the dimer excitations to hop and develop a dispersion. The dispersion of the one-magnon mode produces a bandwidth extending between the gap energy of 3.451(8) meV and the maximum value of 6.84(1) meV as found by inelastic neutron scattering and consistent with magnetization. A second band due to two-magnon excitations was also found centered at 10.5 meV. The inelastic neutron scattering data was fitted to a RPA model based on the dimer unit and the intradimer and interdimer interactions were determined.

Our results can be compared to previous experimental work on $Sr_3Cr_2O_8$. Y. Singh and DC. Johnston[19] measured the DC susceptibility and obtained a value of $J_0 = 5.17(1)$ meV in good agreement with our value. In contrast their value for the sum of the interdimer exchange constants is $J' = 0.5(2)$ meV, which, while consistent with our best fit value from susceptibility, is much smaller than our more accurate value of $J' = 3.6(1)$ meV obtained from inelastic neutron scattering. Inspection of the fitting process shows that the susceptibility data can however be well modeled by a wide range of J' values including $J' = 3.6(1)$ meV.

Chapon *et al.*[20] show from diffraction measurements that $Sr_3Cr_2O_8$ undergoes a Jahn-Teller distortion resulting in a lowering of the crystal symmetry to monoclinic. This distortion would produce spatially anisotropic exchange interactions and result in three twinned domains of equal volume below the phase transition. Our results are consistent with this distortion since we observe three excitation modes arising from the three twins and our fitted exchange interactions are indeed spatially anisotropic. The exchange interactions in

$Sr_3Cr_2O_8$ have been calculated theoretically using the Extended Hückel tight binding model[20] and the theoretical value of J'/J_0 is 0.11, which is much smaller than our experimentally determined value for this ratio of 0.64(2). Finally, Chapon *et al.* used powder inelastic neutron scattering measurements to show that the intradimer interaction is the intrabilayer interaction with a value of $J_0=5.46$ meV in good agreement with our value, however, the size of the interdimer interactions could not be obtain from the bandwidth of the excitations due to the low resolution of the measurement.

Our results can be compared to those for the related compounds $Ba_3Mn_2O_8$ and $Ba_3Cr_2O_8$. The magnetic ion Mn^{5+} has spin-1 compared to spin-1/2 for Cr^{5+}, and is not Jahn-Teller active, as a result $Ba_3Mn_2O_8$ retains hexagonal symmetry down to low temperatures and the interactions remain frustrated. A single one-magnon excitation branch is observed with minima at $(1/3_h, 2/3_h, 1/2_h)$ and equivalent positions.[7] In contrast $Ba_3Cr_2O_8$ like $Sr_3Cr_2O_8$ undergoes a Jahn-Teller distortion to monoclinc symmetry leading to spatially anisotropic exchange interactions and three excitation branches arising from the three twinned domains with minima at the $(1/2_h, 1_h, 0_h)$ etc positions.

The values of intradimer interaction J_0 are smaller in the Ba compounds being 1.64 meV for $Ba_3Mn_2O_8$ [7] and 2.38 meV for $Ba_3Cr_2O_8$.[13] This may simply be due to the intradimer distance which is greater for $Ba_3Cr_2O_8$ (3.934 Å) and $Ba_3Mn_2O_8$ (3.984 Å) than for $Sr_3Cr_2O_8$ (3.842 Å) allowing better overlap of orbitals. The sizes of the interdimer exchange constants are also on average smaller in these compounds although the ratio of intradimer to interdimer couplings is larger. In $Ba_3Cr_2O_8$ $J'=1.94$ meV, and $J'/J_0=0.8151$ while for $Ba_3Mn_2O_8$ $J'/J_0=0.6983$ showing that the ratio of excitation bandwidth to the average mode energy is greater than in $Sr_3Cr_2O_8$ where $J'/J_0=0.64(2)$. Finally the spin gap of $Sr_3Cr_2O_8$ is 3.451(8) meV and is thus significantly larger than that of $Ba_3Mn_2O_8$ (1.08 meV) and $Ba_3Cr_2O_8$ (1.38 meV).

Plenty of additional work on $Sr_3Cr_2O_8$ is needed to fully understand this system. Optical absorption measurements are currently underway to measure the orbital energy level diagram and test the orbital ordering proposed by Chapon *et al.*[20] EPR is also taking place to determine the g tensor and to search for higher order terms in the Hamiltonian e.g., Dzyaloshinskii-Moriya interactions.[14] We also plan Raman scattering measurements to further investigate the magnetic excitation spectrum, and magnetostriction measurements to study the magneto-elastic coupling. Finally, $Sr_3Cr_2O_8$ is a candidate compound for Bose-Einstein condensation of magnons, where an applied magnetic field of $H_c=30.9(4)$ T is required to close the spin gap and start condensing magnons in the ground state, while full saturation is achieved at a field of $H_s=61.9(3)$ T. In fact the phase diagram of $Sr_3Cr_2O_8$ has recently been mapped out using heat capacity and the magnetocaloric effect measurements.[16] The extracted critical exponent of the ordering temperature as a function of reduced field around H_c is indeed in agreement with the universality class predicted for a three-dimensional Bose-Einstein condensate and measurements of the critical exponents at the upper critical field are in progress.

ACKNOWLEDGMENTS

We acknowledge Y. Singh and D. C. Johnston for their help with the preparation for powder samples and D. N. Argyriou for the use of the Crystal laboratory at HZB. R. A. Ewings and T. G. Perring provided the Horace program along with their expertise for viewing and analyzing the Merlin data. T. Herrmannsdörfer provided valuable advice and expertise on the magnetization measurements.

*diana.quintero_castro@helmholtz-berlin.de

[1] C. Ruegg, N. Cavadini, A. Furrer, H. U. Gudel, K. Kramer, H. Mutka, A. K. Habicht, P. Vorderwisch, and A. Wildes, Nature (London) **423**, 62 (2003).
[2] T. Nikuni, M. Oshikawa, A. Oosawa, and H. Tanaka, Phys. Rev. Lett. **84**, 5868 (2000).
[3] Y. Sasago, K. Uchinokura, A. Zheludev, and G. Shirane, Phys. Rev. B **55**, 8357 (1997).
[4] C. Ruegg, D. F. McMorrow, B. Normand, H. M. Ronnow, S. E. Sebastian, I. R. Fisher, C. D. Batista, S. N. Gvasaliya, C. Niedermayer, and J. Stahn, Phys. Rev. Lett. **98**, 017202 (2007).
[5] C. Ruegg, A. Furrer, D. Sheptyakov, T. Strassle, K. W. Kramer, H. U. Gudel, and L. Melesi, Phys. Rev. Lett. **93**, 257201 (2004).
[6] H. Kageyama, K. Yoshimura, R. Stern, N. V. Mushnikov, K. Onizuka, M. Kato, K. Kosuge, C. P. Slichter, T. Goto, and Y. Ueda, Phys. Rev. Lett. **82**, 3168 (1999).
[7] M. B. Stone, M. D. Lumsden, S. Chang, E. C. Samulon, C. D. Batista, and I. R. Fisher, Phys. Rev. Lett. **100**, 237201 (2008).
[8] M. B. Stone, M. D. Lumsden, Y. Qiu, E. C. Samulon, C. D. Batista, and I. R. Fisher, Phys. Rev. B **77**, 134406 (2008).
[9] H.-J. Koo, K.-S. Lee, and M.-H. Whangbo, Inorg. Chem. **45**, 10743 (2006).
[10] M. Uchida, H. Tanaka, M. I. Bartashevich, and T. Goto, J. Phys. Soc. Jpn. **70**, 1790 (2001).
[11] S. Suh, K. Alhassanieh, E. Samulon, J. Brooks, W. Clark, P. Kuhns, L. Lumata, A. Reyes, I. Fisher, S. Brown, and C. Batista, arXiv:0905.0718 (unpublished).
[12] E. C. Samulon, Y. Kohama, R. D. McDonald, M. C. Shapiro, K. A. Al-Hassanieh, C. D. Batista, M. Jaime, and I. R. Fisher, Phys. Rev. Lett. **103**, 047202 (2009).
[13] M. Kofu, J. H. Kim, S. Ji, S. H. Lee, H. Ueda, Y. Qiu, H. J. Kang, M. A. Green, and Y. Ueda, Phys. Rev. Lett. **102**, 037206 (2009).
[14] M. Kofu *et al.*, Phys. Rev. Lett. **102**, 177204 (2009).
[15] A. A. Aczel, Y. Kohama, M. Jaime, K. Ninios, H. B. Chan, L. Balicas, H. A. Dabkowska, and G. M. Luke, Phys. Rev. B **79**, 100409(R) (2009).
[16] A. A. Aczel, Y. Kohama, C. Marcenat, F. Weickert, M. Jaime, O. E. Ayala-Valenzuela, R. D. McDonald, S. D. Selesnic, H. A. Dabkowska, and G. M. Luke, Phys. Rev. Lett. **103**, 207203 (2009).
[17] E. Cuno and H. Mullerbuschbaum, Z. Anorg. Allg. Chem. **572**,

95 (1989).
[18] K. Jacob and K. Abraham, J. Phase Equilib. **21**, 46 (2000).
[19] Y. Singh and D. C. Johnston, Phys. Rev. B **76**, 012407 (2007).
[20] L. Chapon, C. Stock, P. Radaelli, and C. Martin, arXiv:0807.0877 (unpublished).
[21] A. T. M. N. Islam, D. Quintero-Castro, B. Lake, K. Siemensmeyer, K. Kiefer, Y. Skourski, and T. Hermannsdorfer, Cryst. Growth Des. **10**, 465 (2010).
[22] R. I. Bewley, R. S. Eccleston, K. A. McEwen, S. M. Hayden, M. T. Dove, S. M. Bennington, J. R. Treadgold, and R. L. S. Coleman, Physica B **385-386**, 1029 (2006).
[23] T. G. Perring, R. A. Ewings, and J. V. Duijn, (2009), http://horace.isis.rl.ac.uk, and unpublished.
[24] D. C. Johnston, *Handbook of Magnetic Materials* (Elsevier Science, Netherlands, 1997), Vol. 10.
[25] M. Gaft, G. Boulon, G. Panczer, Y. Guyot, R. Reisfeld, S. Votyakov, and G. Bulka, J. Lumin. **87-89**, 1118 (2000).
[26] T. Nakajima, H. Mitamura, and Y. Ueda, J. Phys. Soc. Jpn. **75**, 054706 (2006).
[27] P. Hohenberg and W. Brinkman, Phys. Rev. B **10**, 128 (1974).
[28] A. Furrer and H. U. Gudel, Phys. Rev. Lett. **39**, 657 (1977).